Slip-Ring Induction Motor Torque and Current Ripple Minimization Using Bang-Bang Current Control

EMAR, WALID
Department of Communications and Electronics Engineering, Isra University

Al-Omari, Zakaria
Department of renewable energy engineering, Isra University

Rawashdeh, Taiseer
Department of Architecture Engineering, Isra University

https://doi.org/10.5109/6792891

出版情報：Evergreen. 10 (2), pp.962-975, 2023-06. 九州大学グリーンテクノロジー研究教育センター
バージョン：

EVERGREEN Joint Journal of Novel Carbon Resource Sciences & Green Asia Strategy, Vol. 10, Issue 02, pp962-975, June 2023

Slip-Ring Induction Motor Torque and Current Ripple Minimization Using Bang-Bang Current Control

WALID EMAR[1], Zakaria Al-Omari[2,*], Taiseer Rawashdeh[3]
[1]Department of Communications and Electronics Engineering, Isra University, Amman-Jordan
[2]Department of renewable energy engineering, Isra University, Amman-Jordan
[3]Department of Architecture Engineering, Isra University, Amman-Jordan

*Corresponding author:
E-mail: zakaria.alomar@iu.edu.jo

(Received March 22, 2023; Revised June 1, 2023; accepted June 7, 2023).

Abstract: This paper presents a significant improvement in the dynamic performance and control of an isolated slip-ring induction motor (SRIM). The stator windings of this SRIM-based wound rotor motor are connected to a fixed dc voltage PV system through a boost converter (BC) and a two-level three-phase voltage source inverter (VSI). Thus, SRIM is modulated and controlled using a nonlinear ramp bang-bang current-mode technique (RBBCM) with PWM a modulated inverter VSI. Using Simplorer 7, and MATLAB, the experimental and simulation results are investigated and compared between these techniques.

The results show the following: the improvement, which can be seen by modulating the fixed frequency and waveform achieved by the inverter; The phase shift between the main component of the load phase voltage and current is almost zero; In addition, the variable hysteresis modulation successfully cancels noise and disturbances while also mitigating both higher and lower-order harmonics. The experimental results are investigated and compared with respect to total harmonic distortion, transient response of SRIM speed and developed torque, and other factors that may affect the SRIM performance.

Keywords: slip-ring induction motor; boost converter (BC); Bang-Bang current mode regulation; robust flux regulation.

1. Introduction

Recently the energy demand is increasing. As a result, other forms of energy must be found to conserve supplies. Extensive research has been performed to assess the effectiveness of alternative energy sources[1, 2]. The systems mentioned above have the potential to reduce the energy shortage and contribute to the development of a sustainable energy system. However, existing power must be used efficiently. For this, the power electronic circuits could be a solution to more effectively utilize existing energy, i.e., renewable energy[3-5].

In this paper, the SRIM-based PV system is, in principle, a machine that is operated as a drive electric motor for mechanical loads. In either case, it can be fed with AC currents either on both sides, stator, and rotor windings simultaneously, or on only one side. Thus, the SRIM is treated as a wound rotor induction machine in which electrical power is fed into the stator circuit, and the rotor circuit is simply short-circuited, and used to drive a mechanical load (drive-train wheel)[6-9].

At the start, SRIM is running with a resistive rheostat that is connected to the rotor circuit. This results in greater voltage induced in the rotor circuit to generate sufficient torque for driving the motor. Similarly, if the rotor terminals are short-circuited or the mechanical load connected to the shaft is decreased, the induced voltage and torque are also decreased. Therefore, the main goal of this paper is to control the torque of the SRIM using RBBCM. In this manner, the adjustment of stator current or voltage waveforms with stator frequency helps control the motor's mechanical speed and electromagnetic torque.

Non-linear bang-bang current controllers for ac drive systems could be used to control both the amplitude and phase of the stator currents. RBBCM technique is well known for its advantages in power reliability, segmentation, and minimized torque and current fluctuations. As in the dc drive, the ac drives current and torque controller represent the inner loops of the complete motion regulators. As such, it should, for necessity, have zero or nearly zero steady-state error[10-12].

Simulation models in MATLAB and SIMPLORER are used to investigate the improvement of the dynamic behavior and characteristics of the proposed system (BC-VSI-SRIM) with the respective RBBCM and FOCC techniques.

2. Two-level three-phase voltage source inverter (VSI)

The basic structure of a bridge DC/AC VSI is shown in Figure 1. It has three branches, each of which contains double cells of anti-parallel controllable unidirectional switches (IGBT or BJT) and reverses conducting diodes that form what is called a three-phase bridge VSI.

Moreover, in Figure 1, P_{DC} represents the instantaneous power delivered from the DC source to VSI, P_{AC} signifies the power delivered to the AC load by VSI, and P_s denotes the power accumulated by the internal AC voltage source of the load[13-16].

2.1.Switched model of two-level VSI

To avoid unnecessary details, the transistors or diodes are considered in this paper to be ideal with zero turn-on voltage and zero dynamic resistance during on-regime and behave as an open circuit in the off-regime. The gating signals S_a, S_b, S_c, and $\bar{S}_a, \bar{S}_b, \bar{S}_c$ can be obtained by using suitable pulse width modulation (PWM) technology from several modulation strategies that are widely used in industrial applications of VSI.

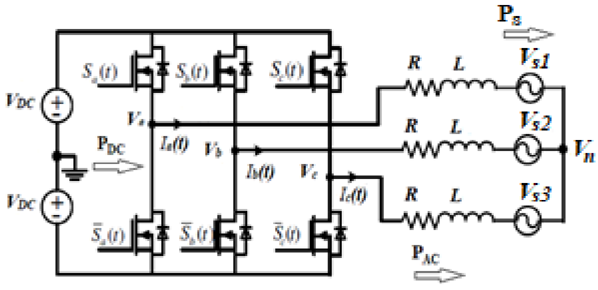

Fig. 1: Schematic diagram of an ideal three-phase two-level VSI with three-phase AC load.

Concerning the waveform of AC terminal phase voltage, $V_{AC}(V_a, V_b, V_c)$, it is dependent on the switching functions used in the adopted macro-technique. Hence, $V_{AC} = V_{DC}$ when an upper transistor or upper diode is on, and $V_{AC} = -V_{DC}$ when a lower transistor or lower diode is on. Applying this for branch (a), yields:

$$
\begin{aligned}
V_a(t) &= (V_{DC})S_a - (V_{DC})\bar{S}_a \\
V_b(t) &= (V_{DC})S_b - (V_{DC})\bar{S}_b \\
V_c(t) &= (V_{DC})S_c - (V_{DC})\bar{S}_c
\end{aligned}
\qquad (1)
$$

$$
\begin{aligned}
i_p &= S_a i_1 + S_b i_2 + S_c i_3 \\
i_n &= \bar{S}_a i_1 + \bar{S}_b i_2 + \bar{S}_c i_3
\end{aligned}
\qquad (2)
$$

$$
S_a + \bar{S}_a = S_b + \bar{S}_b = S_c + \bar{S}_c \equiv 1 \qquad (3)
$$

Where $S_a = S_b = S_c = dT_s$ are the switching states of the upper power electronic cells (transistor-diode pair) and $\bar{S}_a = \bar{S}_b = \bar{S}_c = (1-d)T_s$ are the switching states of the lower power electronic cells. In addition, T_s is the switching period of each branch and d is the duty cycle of each cell that can have any value between zero and one. Equations (1) – (3) describe the switching characteristics for the three-phase bridge VSI. One should notice that the transistor does not necessarily turn on when it is commanded to conduct; the transistor operates only if the on-switching command is provided, and the current direction corresponds to the characteristics of the transistor[17-20].

According to the switching technique used in this paper, the switching states of the upper and lower cells of each branch of the three-phase bridge VSI depend on the flow direction of the load phase current with which the corresponding branch is interfaced. In general, the lower cells do not conduct when the load phase current is positive. On the contrary, the upper cells conduct only positive currents.

3. Modulation and control technique for BC-VSI-SRIM

The variable frequency drive directly connected to the photovoltaic system through BC is modulated and controlled using first the non-linear technique (RBBCM) technique. For better clarification, two topologies of the bang-bang controller-based PWM technique for the two-level VSI are developed in the next section. These topologies are divided into linear and non-linear hysteresis current techniques[9].

3.1.Double-band linear Bang-Bang Current Mode (BBCM) control technique

Figure 2a shows a generalized block diagram of a linear bang-bang current mode regulation for a three-phase VSI. From this figure, the regulation of the stator current of SRIM is separated from the modulation of VSI, so that the operation of the regulator does not depend on the VSI inverter topology. This ensures a constant switching frequency modulation irrespective of the reference current waveform.

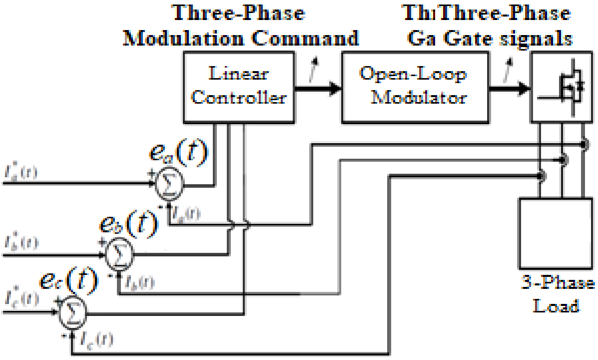

Fig. 2a: Schematic block diagram of linear hysteresis current controlled PWM VSI[12]

The simulation is shown in Figure 2b for the load currents and voltages of a single-phase bridge VSI. Based on the circuit of Figure 1 with the simulation of Figure 2b, one obtains the following relation for phase (a)[12]:

$$L\frac{\Delta I_a}{dt} = V_{ab} - V_{s1} \qquad (4)$$

Where, V_{ab} can consider only the values of $\pm V_{DC}$, based on the power switch's state frequency. Moreover, if the ideal relation sinusoidal current I_a^* is expected to flow in a phase (a) from VSI, the required phase voltage V_{AC}^* of phase (a) would be offered as:

$$L\frac{\Delta I_a^*}{dt} = V_{AC}^* - V_{s1} \qquad (5)$$

Thus, the current error ζ_a is obtained by the following equation

$$\zeta_a = I_a^* - I_a \qquad (6)$$

After rearranging and substituting from Equation 6 into Equation 5, one gets the following relation for the current error during one complete cycle.

$$V_{AC}^* - V_{ab} = L\frac{\Delta(I_a^* - I_a)}{dt} = L\frac{\Delta(\zeta_a)}{dt} \qquad (7)$$

Based on Equation 7, the current error during the on-time of upper switches of the branch (a) of Figure 1 can be expressed mathematically as follows:

$$V_a^* - V_{DC} = L\frac{\Delta(\zeta_a)}{dt} = L\frac{h_{max} - h_{min}}{t_{on}} = L\frac{-h}{t_{on}}, \qquad 0 \le t \le t_{on} \qquad (8)$$

And:

$$(V_a^* + V_{DC}) = L\frac{\Delta(\zeta_a)}{dt} = L\frac{h_{min} - h_{max}}{t_{off}} = L\frac{h}{T_s - t_{on}}, \qquad t_{on} \le t \le T_s \qquad (9)$$

Finally, rearranging Equations (8) and (9) results in the following expression for the switching frequency, f_s:

$$f_s = \frac{V_{DC}^2 - V_a^{*2}}{2h\,L\,V_{DC}} \qquad (10)$$

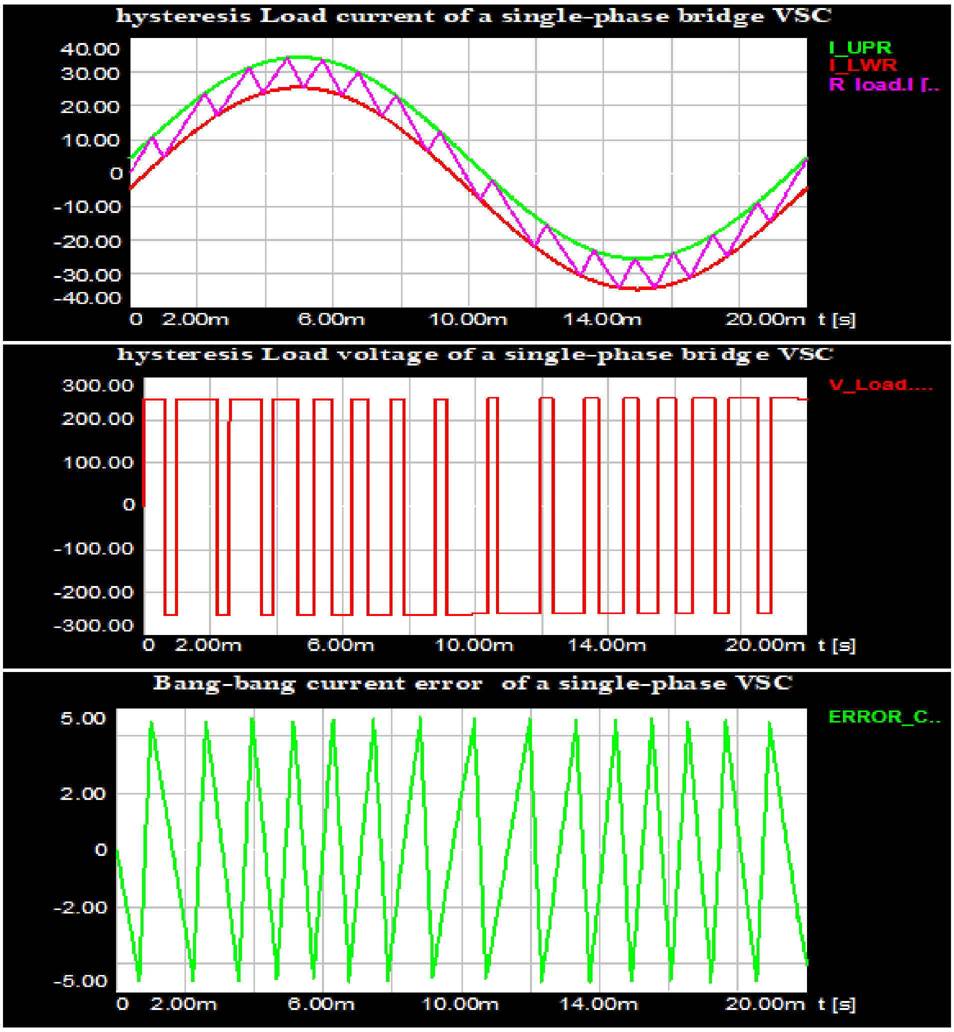

Fig. 2b. Double band Bang-Bang Hysteresis ` Error, Voltage, and Currents Waveforms with RL load for a single-phase VSI.

Where T_s is the switching period of the "triangular signal", the reciprocal of the switching frequency, f_s, and h is the hysteresis window. Equation (10) shows that the switching frequency is dependent on the desired AC terminal voltage and the DC input voltage. It can be noticed how the hysteresis window, h, can be varied in accordance with the required AC terminal voltage just to achieve a constant switching frequency. From equation (10), one may get for the hysteresis window the following expression:

$$h(t) = \frac{V_{DC}^2 - V_a^{*2}}{2\, f_s\, L\, V_{DC}} \qquad (11)$$

Thus:

$$h(t) = h_{max}(1 - \frac{V_a^{*2}}{V_{DC}^2}) \qquad (12)$$

Where $h_{max} = \frac{V_{dc}}{4\, L\, f_s}$ is the maximum possible hysteresis window. In order to achieve the required VSI constant switching frequency, the maximum possible hysteresis window,h_{max}, should be set as a function of the DC-side voltage, V_{DC}.

The double-band Bang-Bang phenomenon for a two-level three-phase VSI is shown in Figure 2c. For a balanced three-phase AC system, the current error summation of all phases should be always zero.

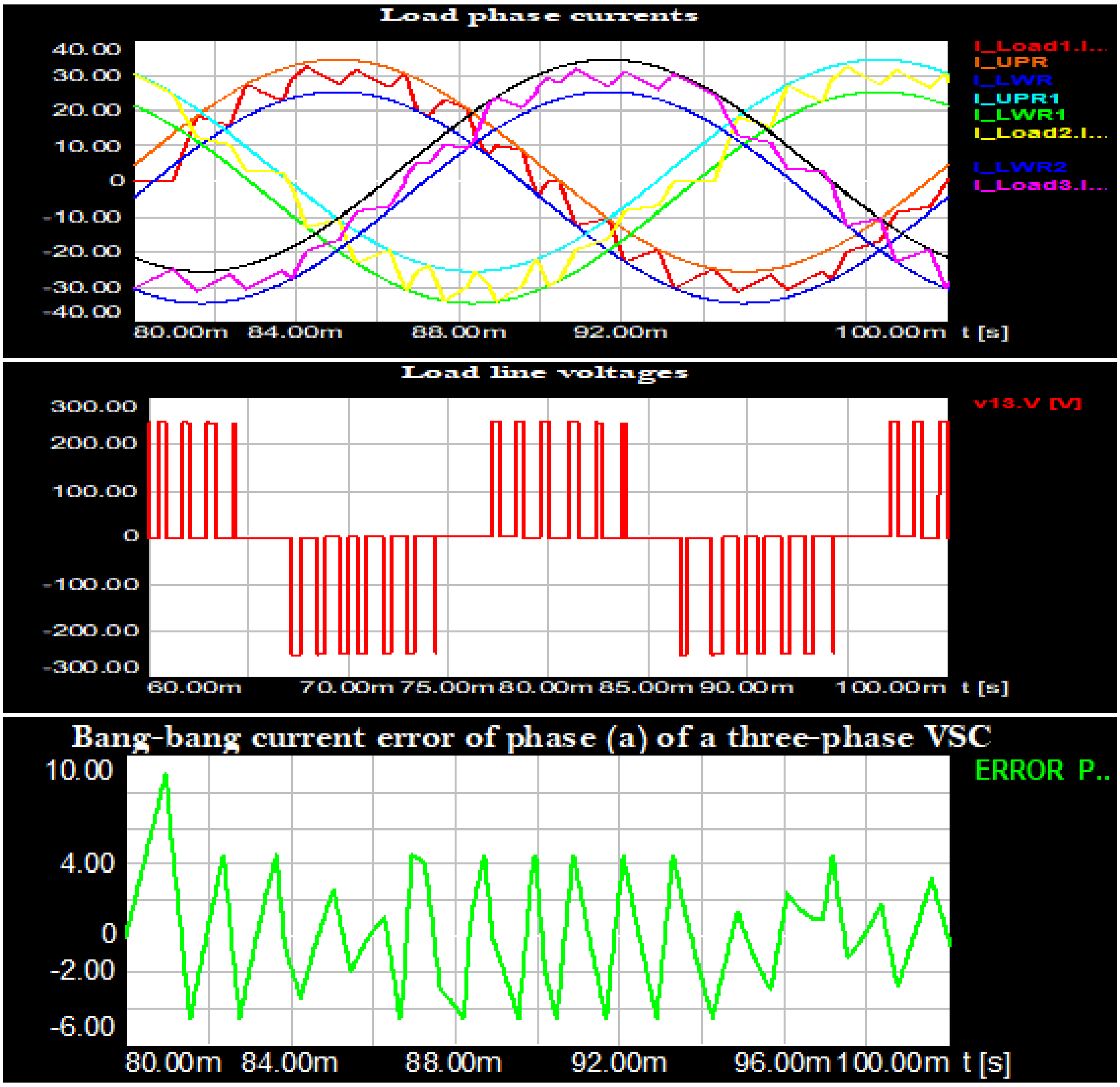

Fig. 2c: Double band Bang-Bang Hysteresis Current Error, Voltage, and Currents Waveforms with RL load for a three-phase VSI.

3.2.Nonlinear RBBCM for VSI

The nonlinear bang-bang-based PWM control of VSI combines the task of the VSI PWM modulation with the non-linear bang-bang current mode regulation of the VSI-SRIM system as shown in Figure 3a. The current error is generated by comparing the desired output current of VSI with the actual current of these conversion processors. The current error is then compared against a constant frequency constant amplitude triangular signal using a hysteresis comparator and limiter interfacing circuit to generate the appropriate gating signals. The primary advantage of triangular RBBCM against the conventional

BBCM is that it represents the desired current error but in the form of a triangular signal that has a constant/variable amplitude and a constant/variable switching frequency. Thereby, both the torque and speed of SRIM could be controlled by a dedicated control scheme through the adjustment of the DC-side voltage and current parameters, in addition to the phase angle and the amplitude of the SRIM stator current with respect to the DC-side voltage[21].

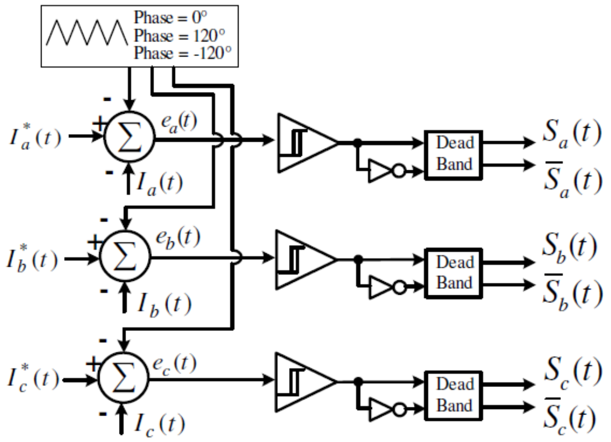

Fig. 3a: Schematic diagram of a non-linear BBCM-PWM with a triangular carrier signal for the two-level three-phase VSI.

Variation of the hysteresis window in a sinusoidal manner based on the regulation of the average value of the internal ac voltage of SRIM or the DC voltage at the DC-side of VSI can result in a constant frequency operation of VSI.

The proposed hysteresis window strategy can be considered as an exemplar visualization of the state-of-the-art for variable hysteresis current modulation techniques. It is mathematically expressed for one phase of a three-phase VSI as:

$$h_a = h_{max}\left[1-\left(\alpha\, V_a(t)+\beta\,\frac{d\zeta_a}{dt}\right)^2\right] \tag{13}$$

Where $\alpha = \frac{1}{V_{dc}}$, $\beta = \frac{L}{V_{dc}}$.

For this strategy, the triangle current error area within a switching cycle may be divided into positive and negative trips and the regulator must ensure that the last and current trip areas are identical. This results in a constant switching frequency regardless of the reference current waveform[21]. Figure 3b represents a RBBCM for one phase of a three-phase system in which i_{abc} is the control input, and V_{abc} is the disturbance input. Again, as shown in Figure 3c, the current error summation of all phases should be always zero. Hence, the current error and instantaneous values of any two-phase current error could be different from the third one and are either at the maximum or the minimum value of the hysteresis window.

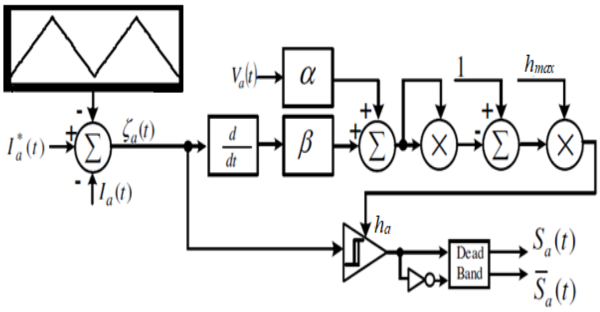

Fig. 3b: Basic block diagram for a per-phase ramp BBCM for a two-level three-phase VSI.

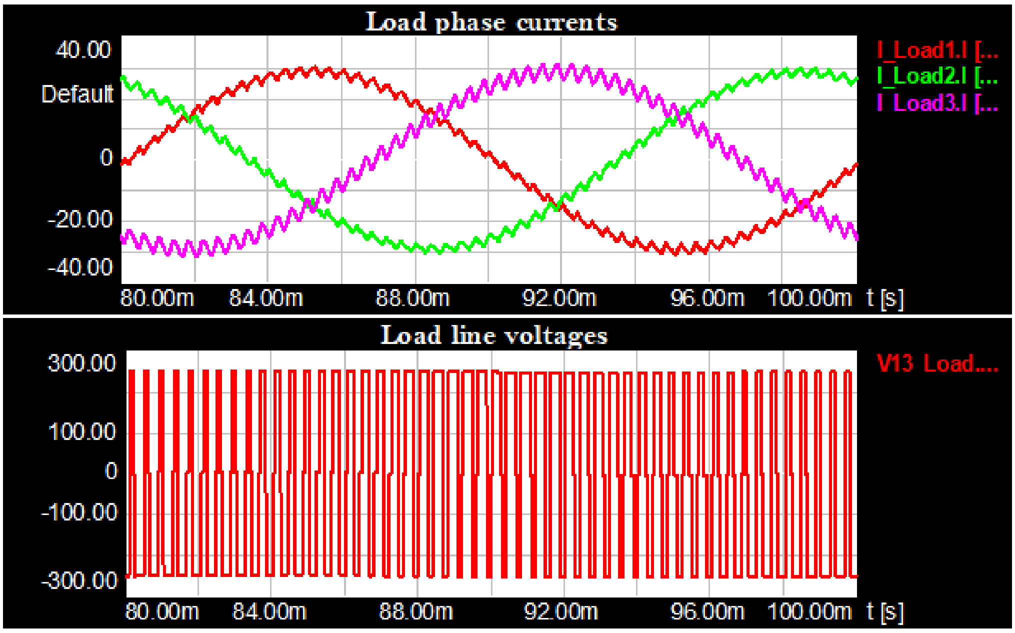

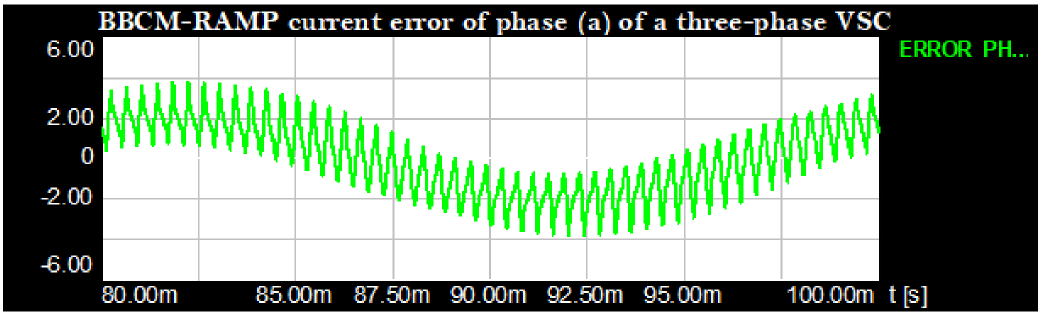

Fig. 3c: BBCM-RAMP Hysteresis Current Error, Voltage and Currents Waveforms with RL load, switching frequency $f_s = 2500Hz$.

4. Performance and control strategy of SRIM with VSI and BC

The performance of the SRIM is tested with a BC processor and field-oriented control regulators for different reference speed conditions and at no-load. The simulation parameters for the SRIM with the mechanical load (drive-train wheel) are listed in Table 1. The operating conditions are explained for convenience as the switching frequency, output voltage, and current rather than motor speed and load torque[22-24].

The mathematical model with a simple per-phase equivalent circuit for Fig. 4a is represented and explained in[22].

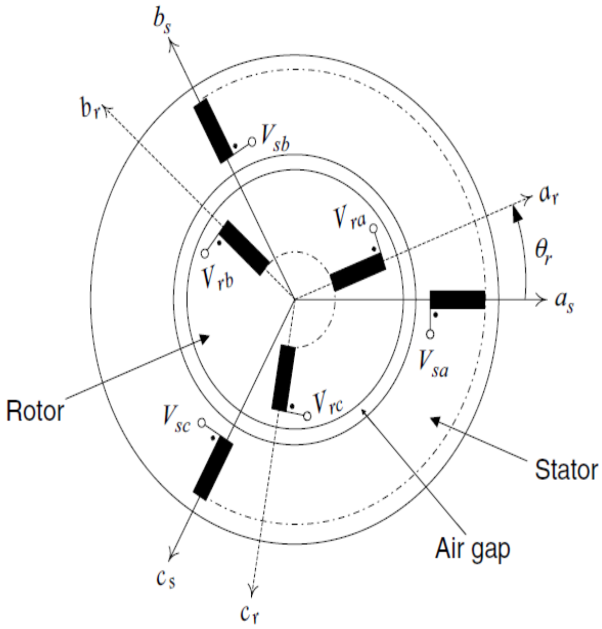

Fig. 4a: Three-phase stator and rotor windings of an AC motor

The mathematical model of the three-phase IM is represented by a set of differential equations and formulated in two forms, stationery, and synchronously rotating reference frames [25-26]. These models will be the mathematical base to build the software that simulates the operation of the motor.

Figure 4b illustrates a direct field orientation control block diagram for torque, flux, and speed control. The measured flux in the airgap is the resultant or mutual flux. By measuring the stator q and d-current components, one can determine the value of the angle ρ and the magnitude of the rotor flux.

$$i_{ds}^{s} = \frac{1}{\sqrt{3}}(i_{cs} - i_{bs})$$
$$i_{qs}^{s} = \frac{2}{3}i_{as} - \frac{1}{3}i_{bs} - \frac{1}{3}i_{cs} \qquad (14)$$

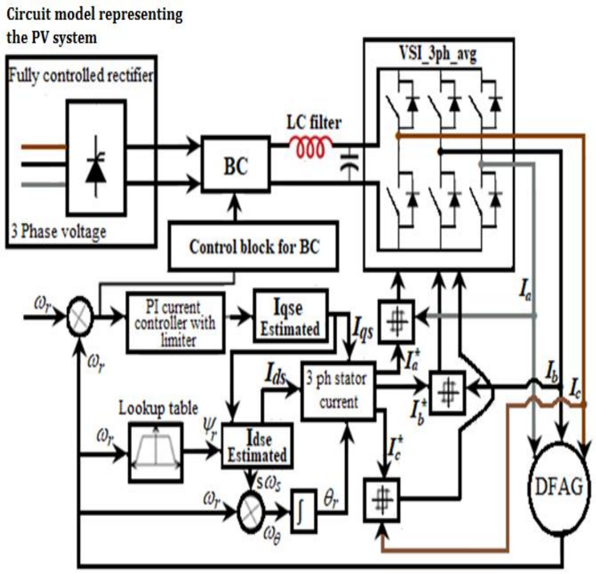

Fig. 4b: The proposed field-oriented control block diagram of PV-BC-VSI-SRIM.

Adding and subtracting a $L'_{lr} i^{s}_{qs}$ term to the right-hand side, the rotor q-axis flux linkage in the stationary reference frame may be expressed as:

$$\lambda'^{s}_{qr} = (L_m + L'_{lr} - L'_{lr}) i^{s}_{qs} + (L_m + L'_{lr}) i'^{s}_{qr} \qquad (15)$$

Since the maximum q-component of the stator flux λ^{s}_{mq} is equal to $L_m(i^{s}_{qs} + i'^{s}_{dr})$, one can determine λ'^{e}_{qr} from the measured quantities, thus:

$$\lambda'^{s}_{qr} = \frac{L_r}{L_m}\lambda^{s}_{mq} - L'_{lr} i^{s}_{qs} \qquad (16)$$

Similarly, λ'^{s}_{dr}can be determined by:

$$\lambda'^{s}_{dr} = \frac{L_r}{L_m}\lambda^{s}_{md} - L'_{lr} i^{s}_{ds} \qquad (17)$$

Using Equations (16) and (17), one can determine the cosine and sine of ρ as follows:

$$\begin{aligned} sin\left(\frac{\pi}{2} - \rho\right) &= cos\,\rho = \frac{\lambda'^{s}_{dr}}{|\lambda'^{s}_{r}|} \\ cos\left(\frac{\pi}{2} - \rho\right) &= sin\,\rho = \frac{\lambda'^{s}_{dr}}{|\lambda'^{s}_{r}|} \end{aligned} \qquad (18)$$

The respective outputs of the torque and flux controllers are the command values, i^{e*}_{qs}, and i^{e*}_{ds}, in the field-oriented rotor reference frame. The resulting frame signals are then converted to phase current commands for the inverter as follows:

$$\begin{aligned} i^{s*}_{qs} &= i^{e*}_{qs}\,cos\,\rho + i^{e*}_{ds}\,sin\,\rho \\ i^{s*}_{ds} &= -i^{e*}_{qs}\,sin\,\rho + i^{e*}_{ds}\,cos\,\rho \end{aligned} \qquad (19)$$

Thus:

$$\begin{aligned} i^{*}_{as} &= i^{s*}_{qs} \\ i^{*}_{bs} &= -\frac{1}{2} i^{s*}_{qs} - \frac{\sqrt{3}}{2} i^{s*}_{ds} \\ i^{*}_{cs} &= -\frac{1}{2} i^{s*}_{qs} + \frac{\sqrt{3}}{2} i^{s*}_{ds} \end{aligned} \qquad (20)$$

where '*' denotes the command desired quantities. The composite control plant, therefore, consists of a subsystem that describes the dynamics of i^{*}_{as}, i^{*}_{bs}, and i^{*}_{cs} as functions of i^{s*}_{qs} and i^{s*}_{ds}. The torque component of the current i^{e*}_{qs} is generated from the speed control loop[27, 28)].

Concerning the developed torque, T^{*}_{em} at the given level of rotor flux, the desired value of this torque is given as follows:

$$T^{*}_{em} = \frac{3}{2}\frac{P}{2}\frac{L_m}{L_r}\lambda'^{e*}_{dr} i^{e*}_{qs} \qquad (21)$$

It has been shown that when properly oriented, i'^{e}_{dr} is zero and $\lambda'^{e}_{dr} = L_m i^{e}_{ds}$: thus, the slip speed relation of SRIM can also be written as:

$$\omega^{*}_{2} = \omega_e - \omega_r = \frac{r'_r}{L'_r}\frac{i^{e*}_{qs}}{i^{e*}_{ds}} \qquad (22)$$

Figure 4b illustrates the control scheme of a bang-bang current-controlled PWM induction motor drive. The field orientation, ρ, is the sum of the rotor angle from the position sensor,θ_r, and the angle,θ_2, from the slip speed. The simulation process considered the operation of 100-hp, 260 V, 50 Hz, and 2poles, with the parameters mentioned in Table 1.

Table 1. Technical Parameters of SRIM with FOCC Control Technique.

Parameter	Symbol	Value
SRIM stator resistance:	R_s	26.37mΩ
SRIM rotor resistance:	R_r	14.14mΩ
SRIM stator leakage inductance:	L_s	0.3676mH
SRIM rotor leakage inductance:	L_r	0.1174mH
SRIM main inductance:	*M*	6.69mH
SRIM moment of inertia	*J*	0.54kg.m^2
Speed controller time constant	*Tiw*	0.54s
Speed controller gain	*Kpw*	10
Torque controller time constant	*TiM*	0.235s
Torque controller gain	*KpM*	10
Current controller time constant (d-component)	*Tid*	18m
Current controller gain (d-component)	*Kpd*	56.37m
Current controller time constant (d-component)	*Tiq*	18m
Current controller gain (d-component)	*Kpq*	56.37m

5. Overall simulation results and performance parameters

The aim of this section is to get acquainted with performance improvement using the results obtained from the experimental simulation. Also, to examine how well such control keeps rotor flux and torque ripple as small as possible during changes in motor shaft speed and load torque, and to observe the effects of changing motor parameters on the current controller performance.

5.1.Simulation results of RBBCM

The test is done for the SRIM fed on a fixed DC source (PV solar system) via a VSI and BC with RBBCM technique and current, speed, and voltage PI controllers, and then for the field-oriented control with PWM modulation technique respectively. The Waveform of the SRIM stator voltages, currents, speed, torques, and harmonic content waveform are shown in Figures 5, 6, and 7 respectively. The simulation parameters for the proposed system are listed in Table 1.

Figure 5a illustrates that the stator currents settle down at 100ms, and rapidly track the desired currents given by the control system as they fluctuate between the upper and the lower hysteresis window limits harmonically. Figure 8a also shows that the current error signal generated due to the RBBCM technique settles down at 100ms at a constant ripple value. The time constant of the motor is about 145ms. As a result of using BC, the output voltage of BC, Vo, reaches a steady-state value of almost 250V at 100ms.

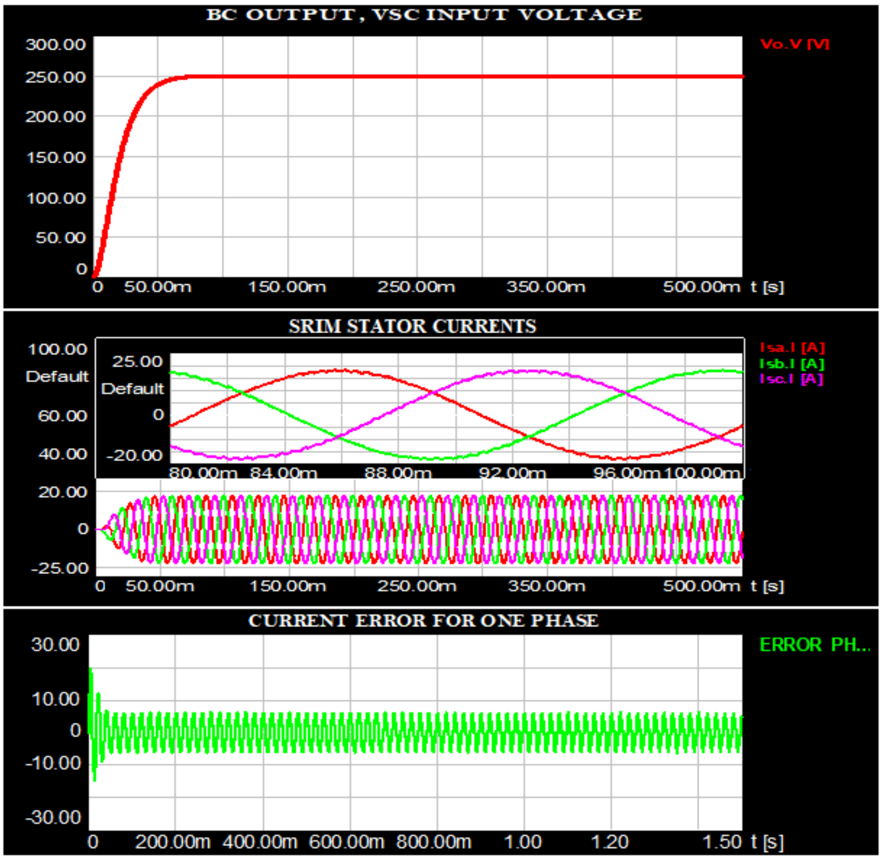

Figure 5a. Stator currents and BC output voltage waveforms with RBBCM current error of one phase with hysteresis current controller.

Figure 5b shows the waveforms of motor-developed torque in green, T_{em}, and the rotor shaft speed in red. The load connected to the SRIM shaft consists of a mechanical drive train with an inertia moment of 0.54-kg.m2. The figure shows that the speed is settled at approximately 400ms. which is the same settling time as the SRIM-developed torque and the load torque. The steady-state value of the speed is 1000rpm.

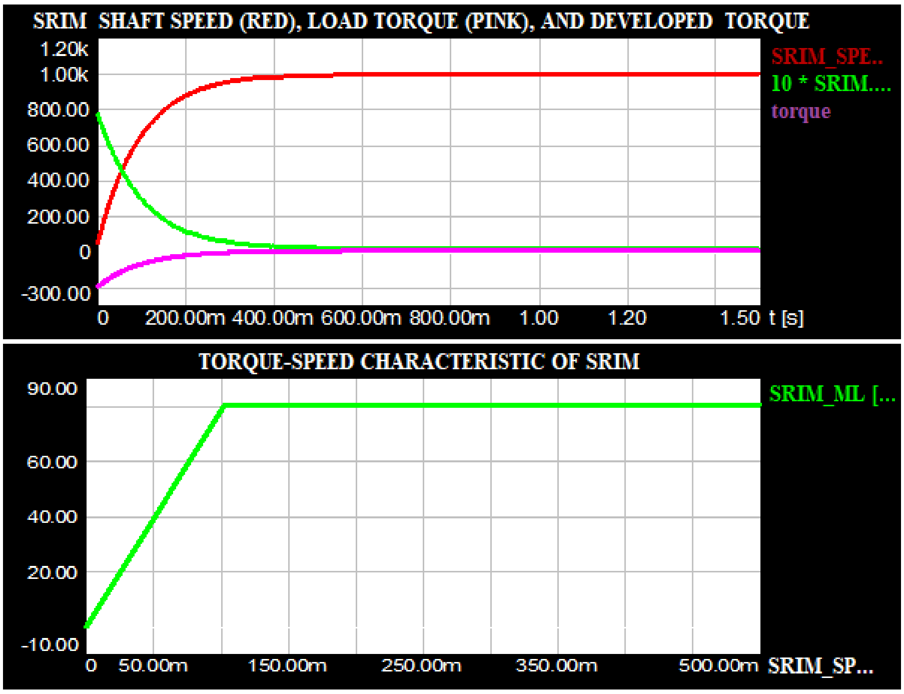

Fig. 5b: SRIM shaft speed, load torque, developed torque, and torque-speed characteristic with hysteresis current controller.

The slow response of the motor speed with the fluctuation in the torque-speed characteristic is due to the exponential increase in the load torque. Therefore, adding speed and current PI controllers to the proposed control scheme produces a compensation of the torque fluctuation based on the speed error and the current error in each phase, which results in reducing the vibration in the torque-speed characteristic. This is verified by the simulation and tests of different parameters of the system as shown in Figure 6a.

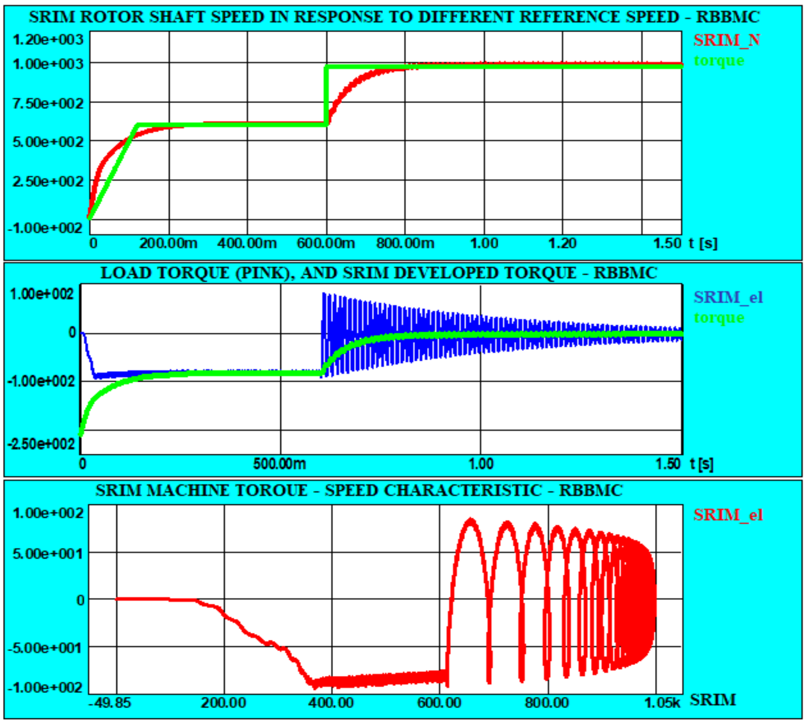

Fig. 6a: SRIM shaft speed, load torque, developed torque, torque-speed characteristic, current error of one phase with hysteresis current and PI controllers

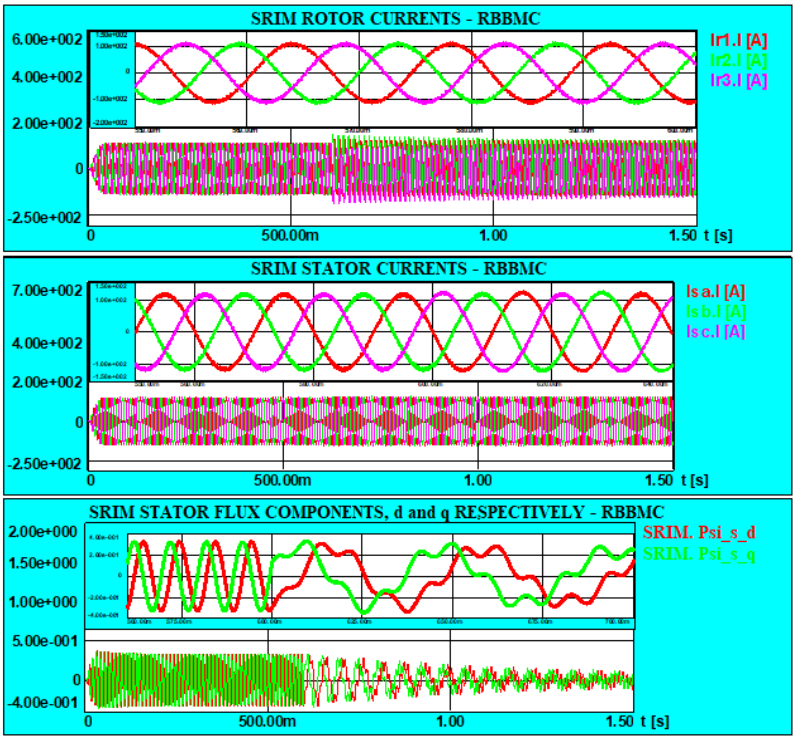

Fig. 6b: Transient and steady-state SRIM stator and rotor currents with the stator flux d- and q- components when the PI controller is employed with the hysteresis current controller.

A comparison of the corresponding results in Figures 5 and 6 shows that the PI compensator is significantly sufficient to ensure an exact following of the SRIM speed, torque, and current response to the applied speed and load torque with satisfactory performance. However, as indicated in Figure 7a, a more complicated compensator (controller) is required to track the sinusoidal current commands and desired speed variation with a high degree of honesty.

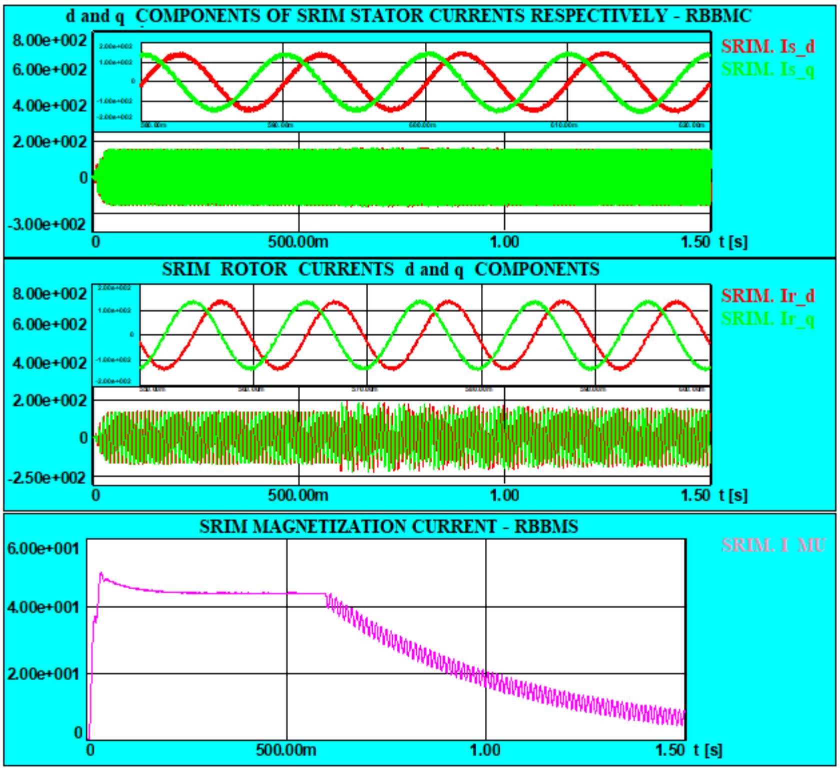

Fig. 6c: SRIM stator and rotor d- and q- current components when PI controller is employed.

With the complexity and diversity of low-power applications to large-power applications of SRIM, it may be more efficient to test the SRIM under the field-oriented control (FOCC) with parameters of SRIM mentioned in Table 1 to see the behavior differences of SRIM.

5.2.RBBCM as compared to field-oriented control technique (FOCC)

Concerning the field-oriented control method, controlling stator current is more straightforward than controlling stator voltage. With proper DC bus voltage and fast switching devices, direct control of stator current can be easily achieved, as shown in the following simulation. The following assumptions were made for the simulation purposes[29):

- The stator windings are connected in a star configuration.
- The saturation is not considered.
- SRIM is operated as a wound-rotor induction motor.

The flux measured in the air gap is usually the mutual flux. It is not the same as the flux that links the rotor winding, whose angle, ρ, is the desired angle for the orientation of the field. The value of the angle ρ and the magnitude of the rotor and stator fluxes are determined from the measured stator currents. The measured abc stator currents are first transformed into qd stationary current components using the Clerk and Park transformations[20-22).

Figure 7a illustrates the dynamic behavior of SRIM in response to the exponential change of the load torque due to the commands of FOCC. Based on the unified model of the FOCC, presented in this paper, there is no big difference between the dynamic response of the SRIM due to the FOCC controller and that of RBBCM. A comparison of Figures 6 and 7 confirms this. Figures 6 and 7 show the motor speed does not change with the variation in the load torque and exactly follows the command signals.

The FOCC control system parameters are the same as those of RBBCM, and the proposed system of SRIM is subjected to the same sequence of disturbances. Thus, a comparison of Figures 5 and 6 with Figures 7 indicates that the SRIM speed with the FOCC control technique settles down at 120ms which is faster than that of the RBBCM technique depicted in Figure 6. In the FOCC control system of Figure 7b, following the disturbance and variation of the desired speed, the torque-speed characteristic of SRIM with FOCC has a better waveform and is not permitted to fluctuate further as the speed reaches its steady value. However, under the FOCC injected PWM, the SRIM speed response to two different reference speeds can reach its final steady-state speed faster than that of RBMMC, but with a significant offset. This offset could be eliminated using an appropriate control parameter.

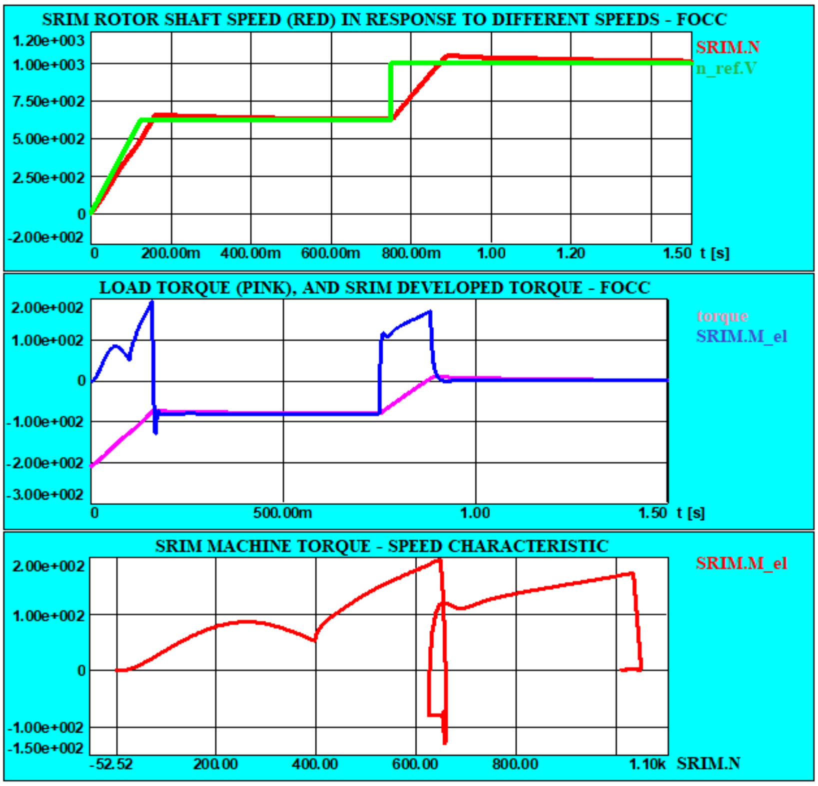

Fig. 7a: SRIM shaft speed, load torque, developed torque, and torque-speed characteristic with FOCC controllers.

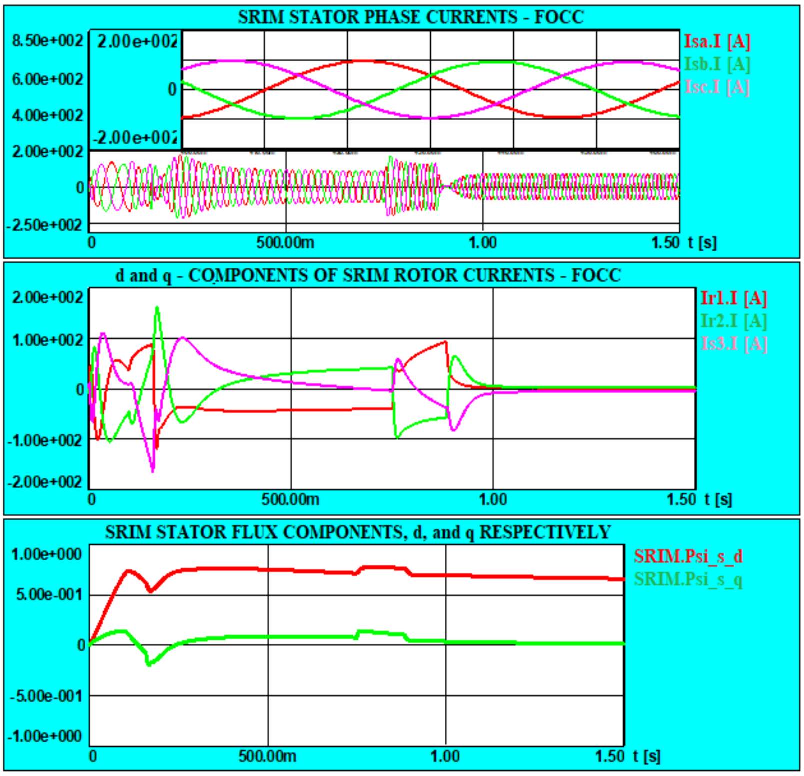

Fig. 7b: Transient and steady-state SRIM stator and rotor currents with the stator flux (d- and q- components) when the FOCC controller is employed.

Further comparison between Figures 5 and 6 with Figures 7 reveals that the FOCC control technique injected PWM generates an acceptable waveform of the stator currents in Figure 7b as compared to that of RBBCM in Figure 6b. Figure 7b indicates that the SRIM with the FOCC-injected PWM exhibits an unexplainable waveform of the currents of the short-circuited rotor as compared to the waveform of rotor currents shown in Figure 6b.

One can see from Figure 6a the similarity in the response of the machine-developed torque to the applied load torque compared to the one in Figure 7a. Also, how well the flux stator flux components (d and q) remain constant in Figure 7b when the motor is loaded as compared to the flux response in Figure 6a.

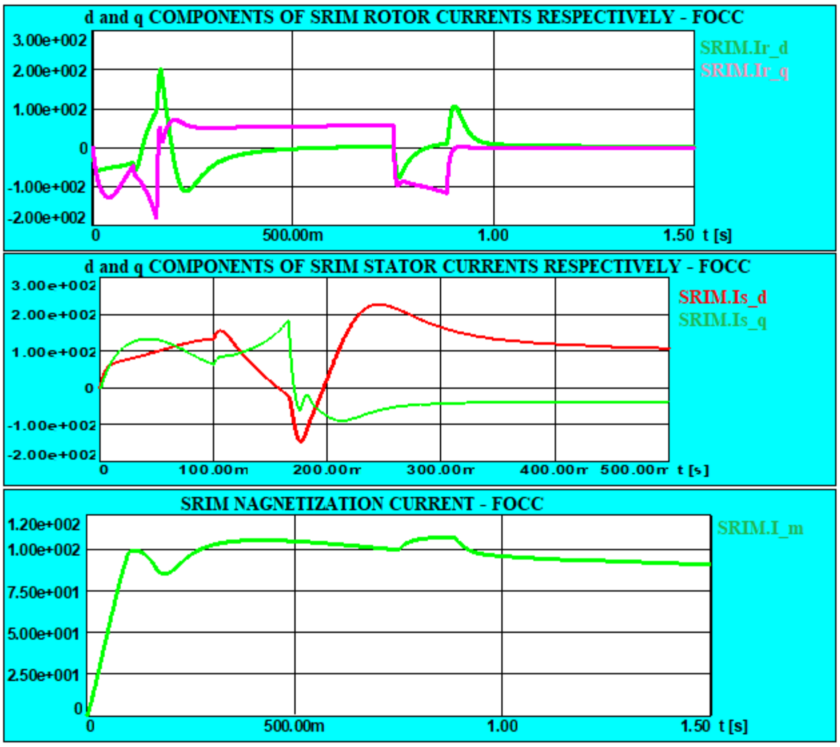

Fig. 7c: SRIM stator and rotor d- and q- current components when FOCC is employed.

Another comparison is clear between the stator respective rotor current responses (d and q) of Figure 6c and Figure 7c. In Figure 6c, the rotor and stator (d and q) current components show a smooth sinusoidal response in the case of RBMMC with PI controller, while it is oscillatory in the case of FOCC as shown in Figure 7c. The related d and q current components in the simulation give significant evidence about the appropriate control principle of the SRIM in the appropriate application.

6. Conclusion

A PV-power dc source is designed, simulated, and analyzed using a BC and two-level three-phase VSI. This configuration was used to power an isolated SRIM, which was then investigated and tested under various operational scenarios.

The SRIM is modulated and controlled using a nonlinear RBBCM with PWM a modulated VSI. Using Simplorer 7, and MATLAB, the experimental and simulation results are investigated and compared between these techniques.

The behavior of the proposed SRIM is tested for various change/frequency indicators and operating conditions under different load and rotor shaft speed values. The SRIM with a mechanical drive train load shows good results under different operating conditions with both techniques, RBMMC and FOCC respectively. The results obtained show the following:

- The improvement, which can be seen by modulating the fixed frequency and waveform achieved by the VSI;
- The phase shift between the main component of the load phase voltage and current is almost zero;
- Furthermore, variable hysteresis modulation effectively cancels noise and disturbances while mitigating both higher and lower-order harmonics.

The experimental and simulation results show that the RBBCM control technique has the potential to improve the closed-loop control performance of variable-speed drive systems. In addition, the proposed RBBCM scheme virtually needs no machine parameters compared to conventional FOCC drive systems. Therefore, the

RBBCM makes the speed control of the FOCC variable speed drive systems robust and practical.

References

1) Indri Yaningsih, et al, "Numerical study on the Effect of Rectangular and Triangular Counter-Rotating Vortex Generators on the H-Rotor Wind Turbine Performance," *EVERGREEN Joint Journal of Novel Carbon Resource Sciences & Green Asia Strategy*, **10** (01), 230-241 (2023). https://doi.org/10.5109/6781073
2) M. W. AlShaar, Z. Al-Omari, W. Emar, M. Alnsour, and Gh. Abu-Rumman, “Application of PV-Thermal Array for Pumping Irrigation Water as an Alternative to PV in Ghor Al-Safi, Jordan: A case study,” *EVERGREEN Joint Journal of Novel Carbon Resource Sciences & Green Asia Strategy*, **09** (04), 1140-1150 (2022). https://doi.org/10.5109/6625725
3) M. Motinur Rahman, et al, "Energy Conservation of Smart Grid System Using Voltage Reduction Technique and Its Challenges," *EVERGREEN Joint Journal of Novel Carbon Resource Sciences & Green Asia Strategy*, **09** (04), 924-938 (2022). https://doi.org/10.5109/6622879
4) L. K. Sagar, and D. Bhagwan Das, “Fuzzy Expert System for Determining State of Solar Photo Voltaic Power Plant Based on Real-Time Data,” *EVERGREEN Joint Journal of Novel Carbon Resource Sciences & Green Asia Strategy*, **09** (03), 870-880 (2022). https://doi.org/10.5109/4843118
5) A. Dhiman, and Gulshan Sachdeva, “Energy and Exergy Analysis of a Pressurized Solar Cooking System Based on a Parabolic Dish Collector,” *EVERGREEN Joint Journal of Novel Carbon Resource Sciences & Green Asia Strategy*, **09** (04), 1168-1180 (2022). https://doi.org/10.5109/6625728
6) W. Emar, and Omar A. Saraereh, “Analytical and Comparative Study of Different Types of Two-Leg Chopping up Regulator,” *International Journal of Advanced Computer Science and Applications*, **10** (5) 115-128 (2019). doi: 10.14569/IJACSA.2019.0100515
7) M. Boufadene, M. Belkheiri, and A. Rabhi, “Adaptive nonlinear observer augmented by radial basis neural network for a nonlinear sensorless control of an induction machine,” I*nternational Journal of Automation and Control*, **12** (1) 27–43 (2018).
8) W. Emar, “Analysis, Modelling and Simulation of step-up Converter using MATLAB Simulink and Simplorer,” *International Journal of Modeling, Simulation, and Scientific Computing*, **7** (3) 1–13 (2016).
9) M. Azzaoui, and H. Mahmoudi, “Fuzzy-PI control of a doubly fed induction generator-based wind power system,” *Int. J. Automation and Control*, **11** (1) 54–66 (2017).
10) Hamdy Mohamed Soliman, "Improve the Performance Characteristics of Induction Motor through Bang Bang Controller," *International Journal of Emerging Technology and Advanced Engineering*, **6** (10) 36-46 (October 2016).
11) Hamdy Mohamed, "Performance Characteristics of Induction Motor with Field Oriented Control Compared to Direct Torque Control," *International Journal of Power Electronics and Drive Systems* **7** (4):1125, (December 2016).
12) W. Emar, “A New Modified Class of SEPIC Converter Processors with PV and A/C Integrated Circuit Systems,” *Journal of Circuits, Systems and Computers,* 30 (10) 2150176 (2021). https://doi.org/10.1142/S0218126621501760
13) T. Qanbari, B. Tousi, M. Farhadi-Kangarlu, “A Novel Vector-Based Pulse-Width Modulation for Three-Phase Two-Level Voltage Source Inverters,” *Journal of Operation and Automation in Power Engineering*, **11** (1) 50-60, (Apr. 2023).
14) C. Dinh et al, “An Improving Hysteresis Current Control Method Based on FOC Technique for Induction Motor Drive,” *J. Adv. Eng. Comput*. **5** (2021): 83.
15) D. C. Pham, "Modeling and simulation of two level three-phase voltage source inverter with voltage drop," *2017 Seventh International Conference on Information Science and Technology (ICIST)*, Da Nang, Vietnam, 2017, pp. 317-322, doi: 10.1109/ICIST.2017.7926777.
16) Jayesh A. Gangurde, Mohan P. Thakre, Comparative Analysis of PWM Overmodulation Techniques in Three Phase Two Level Voltage Source Inverter," *International Conference on Contents, Computing & Communication* (ICCCC-2022).
17) M. Affan, and R. Uddin, “Brain Emotional Learning and Adaptive Model Predictive Controller for Induction Motor Drive: A New Cascaded Vector Control Topology,” *Int. J. Control Autom. Syst.*, **19** 3122–3135 (2021).
18) Wu QM., Y. Zhan, and Zhang, M. et al., “Efficiency Optimization Control of an IPMSM Drive System for Electric Vehicles (EVs),” *Int. J. Control Autom. Syst.*, **19** 2716–2733 (2021).
19) J. N. Chandra Sekhar, and G. V. Marutheswar, “Direct Torque Control of Induction Motor Using Enhanced Firefly Algorithm — ANFIS,” *Journal of Circuits, Systems and Computers*, **26** (06) 1750092 (2017).
20) M. J. Yarmohammadi, M. Taghizadeh, and Sadeghzadeh, “A. LPV Control of Wind Turbine with Hydrostatic Transmission Under Inaccurate Wind Speed Measurement,” *Int. J. Control Autom. Syst.*, **20** 1561–1568 (2022).
21) A. MARTINEZ, Y. KRIM, D. ABBES and B. EKER, " Comparison of Bang Bang and PMW switching techniques for DC/AC photovoltaic converter," *20th*

International Conference on Renewable Energies and Power Quality (ICREPQ'22) Vigo (Spain), 27th to 29th July 2022.

22) M. ELMAHFOUD, B. BOSSOUFI, M. TAOUSSI, N. E. OUANJLI and A. DEROUICH, "Rotor Field Oriented Control of Doubly Fed Induction Motor," *2019 5th International Conference on Optimization and Applications (ICOA)*, Kenitra, Morocco, 1-6 (2019). doi: 10.1109/ICOA.2019.8727708.
23) D. Zhou and R. Spee, "Field oriented control development for brushless doubly-fed machines," *IAS '96. Conference Record of the 1996 IEEE Industry Applications Conference Thirty-First IAS Annual Meeting*, San Diego, CA, USA, 1 (1) 304-310. doi: 10.1109/IAS.1996.557036.
24) C. M. Rahul Charles, V. Vinod, and A. Jacob, “Field oriented control of Doubly Fed Induction Generator in wind power system,” *2015 IEEE International Conference on Computational Intelligence and Computing Research (ICCIC)*, Madurai, India, pp. 1-5 (2015). doi: 10.1109/ICCIC.2015.7435760.
25) Oleksiy Kuznyetsov, " Mathematical Model of a Three-Phase Induction Machine in a Natural abc Reference Frame Utilizing the Method of Numerical Integration of Average Voltages at the Integration Step and Its Application to the Analysis of Electromechanical Systems," *Mathematical Problems in Engineering*, **2019**, Article ID 4581769, 13 pages. https://www.hindawi.com/journals/mpe/2019/4581769/
26) Sengamalai, Usha, Geetha Anbazhagan, T. M. Thamizh Thentral, Pradeep Vishnuram, Tahir Khurshaid, and Salah Kamel. "Three Phase Induction Motor Drive: A Systematic Review on Dynamic Modeling, Parameter Estimation, and Control Schemes," *Energies* **15** (21): 8260 (2022). https://www.mdpi.com/1996-073/15/21/8260
27) Shafiq Odhano, Radu Bojoi, Andrea Formentini, Pericle Zanchetta, Alberto Tenconi, Direct flux and current vector control for induction motor drives using model predictive control theory," *IET Electric Power Applications*, **11** (8) 1483-1491 (2017).
28) Z. Elbarbary, M. F. Azeem, and H. Z. Azazi, “Adaptive Fuzzy-Based IRFOC of Speed Sensorless Six-Phase Induction Motor Drive System,” *Journal of Circuits, Systems and Computers*, **29** (04) 2050062 (2020).
29) KARCHUNG, “SENSORLESS FIELD ORIENTED CONTROL OF THREE-PHASE INDUCTION MOTOR USING FUZZY PI CONTROLLER,” *Thesis for the Master of Engineering in (Electrical Engineering), Naresuan University* (2019).